Received September 26, 2021, accepted October 8, 2021, date of publication November 10, 2021, date of current version January 28, 2022.

Digital Object Identifier 10.1109/ACCESS.2021.3127139

Proposal of Hybrid *N*OAM-MPPM Technique for Gamma-Gamma Turbulence Channel With Pointing Error and Different Deep Learning Techniques

SHIMAA A. EL-MEADAWY[1], HOSSAM M. H. SHALABY[2], (Senior Member, IEEE), NABIL A. ISMAIL[3], FATHI E. ABD EL-SAMIE[1], NAGLAA F. SOLIMAN[4], ABEER D. ALGARNI[4], WALID EL-SHAFAI[1,5], AND AHMED E. A. FARGHAL[6]

[1]Department of Electronics and Electrical Communications Engineering, Faculty of Electronic Engineering, Menoufia University, Menouf 32952, Egypt
[2]Electrical Engineering Department, Faculty of Engineering, Alexandria University, Alexandria 21544, Egypt
[3]Department of Computer Science and Engineering, Faculty of Electronic Engineering, Menoufia University, Menouf 32952, Egypt
[4]Department of Information Technology, College of Computer and Information Sciences, Princess Nourah bint Abdulrahman University, Riyadh 11671, Saudi Arabia
[5]Security Engineering Laboratory, Computer Science Department, Prince Sultan University, Riyadh 11586, Saudi Arabia
[6]Electrical Engineering Department, Faculty of Engineering, Sohag University, Sohag 82524, Egypt

Corresponding author: Abeer D. Algarni (adalqarni@pnu.edu.sa)

This work was supported by the Princess Nourah bint Abdulrahman University Researchers Supporting Project number (PNURSP2022R66), Princess Nourah bint Abdulrahman University, Riyadh, Saudi Arabia.

ABSTRACT A hybrid multi-state orbital angular momentum-multi pulse-position modulation (*N*OAM-MPPM) scheme over gamma-gamma free-space optical (ΓΓ-FSO) channel is studied in this paper. In our study, all atmospheric and pointing error impacts are taken into account. Expressions for the parameters of ΓΓ-FSO-pointing error channel are derived. In addition, approximate-tight upper bounds on the bit-error rates (BERs) of *N*OAM and *N*OAM-MPPM techniques are developed over ΓΓ-FSO-pointing error channels, considering the influences of beam divergence and pointing error (PE). The ΓΓ-FSO-PE channel parameters and the BER expressions are evaluated numerically and verified by simulation. It turned out that the analytical results are nearly the same as those obtained from simulation under different turbulence scenarios and OAM modes. The results demonstrate that under variable turbulence conditions, the *N*OAM-MPPM technique outperforms both ordinary *N*OAM and MPPM systems. Furthermore, different deep learning (DL) techniques, namely random forest (RF), convolution neural network (CNN), and auto-encoder (AE), are employed to get the optimum classification accuracy using different datasets of *N*OAM-MPPM over ΓΓ-PE channel model. Finally, the results indicate that AE has the best performance metrics compared to other models using different datasets.

INDEX TERMS Free-space optic (FSO), multiple pulse-position modulation (MPPM), orbital angular momentum (OAM), pointing error (PE).

I. INTRODUCTION

Orbital angular momentum (OAM) multiplexing is implemented as a flexible technique for transmitting multiple signals through free space optical (FSO) communication channels, similar to mode-division multiplexing (MDM) [1].

The associate editor coordinating the review of this manuscript and approving it for publication was San-Liang Lee.

OAM is an excellent method for co-propagating and maintaining multiple data sources in free space without interference due to the orthogonality of OAM modes [2], [3]. OAM beams are vulnerable to atmospheric turbulence (AT) in real-world communication scenarios, where the random behaviour of the air refractive index induced by irregular pressure and temperature is experienced by spatial variations along the propagation pathway. In the turbulent environment,

the propagation of OAM beams contributes to phase-front distortions as well as beam scattering and wandering [3]. Furthermore, when the power of a signal transmitted by a single OAM mode is transferred to other modes, this is regarded as intermodal crosstalk. Additionally, various OAM modes suffer from various channel losses, such as mode dependent loss (MDL), resulting in device output degradation [4], [5].

Many statistical distributions have been believed and analysed to explain the AT. The log-normal, gamma-gamma ($\Gamma\Gamma$), and exponentiated Weibull (EW) models are the most commonly accepted distributions [6], [7]. The log-normal model is reliable for a point recipient in a weak turbulence environment, according to experimental results [6], [8]. For a point receiver, the $\Gamma\Gamma$ model is widely agreed to be applicable in all turbulence regimes, but this is not the case when aperture averaging is used. The $\Gamma\Gamma$ distribution is a widely used distribution that includes all turbulence regimes ranging from weak to strong. It is the most generalised tractable fading model for describing the AT. It is equivalent to the squared generalised K distribution, with the squared K and double-Rayleigh distributions as special examples [9]. In addition, this model factorizes the irradiance as the product of two separate random processes, each with a gamma PDF, and describes both small- and large-scale atmospheric changes [10]. Moreover, the $\Gamma\Gamma$ model is well-suited with OAM as shown in some references such as [1], [11], and [12].

OAM modes have a Johnson S_B distribution for self-channel irradiance, while crosstalk between OAM modes has an exponential distribution [1]. Since the statistical properties of the S_B distribution are analytically irresolvable, closed-form expressions for output metrics cannot be derived. In addition, since there is no single turbulence model, determining the impact of interference on OAM mode output is difficult [1]. As seen in [6], [13], [14], a more practical scenario has been suggested and investigated, taking into consideration the impacts of divergence and pointing error (PE). Vibrations or building sway can cause pointing errors, which may weaken the optical wireless communication connection.

In recent years, it has been deduced that various modulation techniques can be superimposed simultaneously for enhancing power and spectral efficiencies [6], [15]–[18]. New modulation techniques based on a mixture of M-ary pulse-position modulation (M-PPM) and M-ary frequency-shift keying (M-FSK) have been developed by Liu *et al.* [19]. Hybrid modulation methods have been developed and investigated, combining multi pulse-position modulation (MPPM) with different modulation schemes as shown in [16]–[21].

The conventional OAM-shift keying (OAM-SK) coherent demodulation is ineffective and highly vulnerable to arrival fluctuations and beam wandering [22]. An effective demodulation technique based on an artificial neural network (ANN) has been proposed, where intensity representations of received Laguerre Gaussian (LG) beams are recognized directly, and the corresponding OAM mode information is obtained successfully [11]. Because of the advanced multi-layered representation training, a CNN can directly recognize raw images and discover intrinsic features of inputs without the need for careful feature engineering [11]. Auto-encoder (AE) has proven to be a robust algorithm that can generate unregulated representations in the feature patterns, often more preciseLY [23]. Random forest (RF) is the set of various decision trees that can help avoid over-fitting in each tree and it demonstrates good results [11], [22], [24].

The performance of FSO communication is limited in a turbulent environment, despite its great potential in high capacity, and low power consumption. Scintillation in the FSO propagated signals is created by AT, which increases the BER of the recovered signals at the receiver. The employment of DL detection algorithms could be able to solve these drawbacks. The utilization of DL techniques to recover transmitted data could be an efficient way to use FSO communication in turbulent channels without prior knowledge of the channel conditions [43]. DL has been used in optical communication systems for a variety of tasks, including lowering computational complexity in various optical communication tasks, detecting AT, and developing adaptive algorithms for OAM-based FSO communication.

In this paper, we start by developing channel parameters of a $\Gamma\Gamma$ turbulence channel with PE. Then, taking into consideration the impact of both beam divergence and PE, we use these parameters to study and assess both upper bound and estimated upper bound expressions for the average bit-error rates (BERs) of NOAM, MPPM, and hybrid NOAM-MPPM schemes. In addition, a comparative study between different deep learning (DL) techniques, namely CNN, RF, and AE, is accomplished to determine the optimum model for different datasets of NOAM-MPPM.

The major contributions of this work are:

- Studying the performance of FSO communication over $\Gamma\Gamma$ turbulence channel with PE and deriving the expressions for the various parameters of this channel.
- Developing closed-form expressions for both upper bound and estimated upper bound BERs of NOAM, MPPM, and NOAM-MPPM techniques in the existence of $\Gamma\Gamma$ turbulence FSO channel with PE.
- Achieving a perfect fit between theoretical and simulation results under various turbulence strengths, OAM mode numbers, and SNR values, using Mathematica and MATLAB, respectively.
- Studying the effect of different OAM modes on the efficiency of the NOAM and hybrid NOAM-MPPM models under different AT cases and SNR values.
- Enhancing the detection performance of OAM using different DL models, and studying the performance quality metrics of these models.
- Applying a trial-and-error method to yield the optimum dataset and the most efficient DL model.
- Performing a comparative study between various proposed DL techniques, for determining the optimum model for OAM-SK detection.

- Obtaining the optimum model out of CNN, RF, and AE to get the highest classification accuracy and the lowest root mean-square error (RMSE) for different datasets of NOAM-MPPM-FSO systems.

The remainder of this paper is organized as follows. In Section II, we discuss the related work of hybrid modulation techniques. In Section III, we present the configuration of the proposed NOAM-MPPM model, the parameters of $\Gamma\Gamma$ turbulence with PE channel, and the BER analysis of NOAM and NOAM-MPPM systems. In Section IV, we explain three DL techniques, namely CNN, AE, and RF, and use them to enhance the classification performance. Finally, Section V is the conclusion.

II. RELATED WORK

In [1], closed-form expressions for the outage probability, and BER of the generalized gamma distribution have been studied and derived for SISO transmission. This study effectively models the self-channel fading between OAM modes. To characterise the attenuation and crosstalk in a vortex-based multi-channel FSO communication system, a unique statistical model linked to turbulence strength was provided in [25]. This statistical model was also used with an OAM-multiplexing FSO system with QPSK modulation, and the theoretical average BER results match well with the Monte Carlo simulation results. This work can be used to investigate FSO time-varying systems that use OAM modulation.

In a vortex-based multi-channel laser communication connection, the effect of optical turbulence on energy crosstalk among constituent OAM states was investigated and the channel interference was determined in terms of turbulence strength and OAM state separation [26]. Turbulence-induced channel interference appears to be mutually correlated throughout receive channels.

An alternative effectual CNN architecture designed on the basis of a trial-and-error method has been used to get the values of the optimum network parameters and hyper-parameters [27]. These parameters and hyper-parameters have been used to yield the highest accuracy and mean average precision (MAP), as well as the largest area under the curve (AUC) for different optimizers. To correct and improve the mode purity of the distorted vortex beam from 39.52% to 98.34% under heavy AT, an AT correction approach based on DL has been suggested in [28]. In [22], the mathematical expression for the BER of OAM has been developed over the $\Gamma\Gamma$ turbulence channel. After that, a comparison between the analytical and the simulation results for different AT strengths, ranges, and SNR values has been presented to assure that there is a complete matching. In [11], [29], empirical mathematical expressions have been obtained for the BER of QAM and PSK-OFDM-FSO systems, taking into account the fading impact, which has been modeled by a $\Gamma\Gamma$ distribution. In [30], under the EW distribution, an estimated expression for the symbol-error rate (SER) of MPPM has been developed. The effects of fog, PE, and beam divergence have been neglected. In [6], mathematical expressions have been obtained for the BER of QAM-MPPM through an EW fading AT channel. It has been shown that OAM beams made by imprinting only a helical phase parameter are not suitable for AT-impaired functional OAM-FSO systems. Regulating the original beam-field intensity can also help to reduce OAM beam scrambling [31].

In terms of the Meijer G function, closed-form expressions for the cumulative distribution function (CDF) and probability distribution function (PDF) of the end-to-end mixed radio frequency (RF)/FSO system are developed taking into consideration the PE [32]. In addition, the numerical and Matlab results have been provided to support the developed formulas. High SNR approximations have been offered to provide more insight on the UAV-assisted solution for space-air-ground integrated networks (SAGIN). Furthermore, in the existence of the non-PE effect, approximate equations for the outage probability and average BER have been given in [33]. Finally, Monte-Carlo simulations have been used to validate all of these analytical results. To characterise the turbulence under weak-to-strong conditions, both the lognormal and Gamma-Gamma channel models have been used in [34]. In addition, under the impact of background noise, thermal noise, and quantum noise, the average BER and average channel capacity of an FSO communication system have been evaluated. Thermal noise has a major effect on the FSO system, according to simulation results. Some research work has been done to investigate the effect of the isotropic weak-to-strong oceanic turbulence on the performance of underwater optical communication (UWOC) systems [35]. Simulation results indicate that the parameters of oceanic turbulence have a considerable influence on both outage probability and average channel capacity. The accuracy of the formulations for outage probability and average channel capacity has been verified numerically, and a complete agreement has been proved.

III. NOAM-MPPM SYSTEM THROUGH $\Gamma\Gamma$ CHANNEL WITH PE

In this part, a detailed setup and a configuration block diagram of NOAM-MPPM-$\Gamma\Gamma$ turbulence channel with PE transmission system are presented and explained. In addition, a mathematical expression for the parameters of $\Gamma\Gamma$ turbulence channel plus PE distribution is obtained. Furthermore, the BERs of both NOAM and NOAM-MPPM in FSO transmission channels are developed.

A. NOAM-MPPM SYSTEM

Fig. 1 indicates the fundamental schematic block diagram of the NOAM-MPPM scheme using the $\Gamma\Gamma$ turbulence channel with PE for both transmitter and receiver. At the transmitter side, a frame of $Q_{MPPM+NOAM} = Q_{MPPM} + Q_{NOAM} = \left\lfloor \log_2 \binom{M}{\omega} \right\rfloor + \omega m$ bits is sent to the transmitter signal-processing unit (T-SPU), where $\lfloor y \rfloor$ is the

largest integer not greater than y, M is the number of MPPM time slots ($M = 8$), ω is the number of signal time slots ($\omega = 4$) within M, $m = \log_2(N)$, and N is the constellation of NOAM technique. The bits are manipulated by the T-SPU to control all NOAM and DC-bias level operations, which are used to make the amplitude of OAM positive only. The MPPM algorithm divides a signal frame of duration T_b into M equal time slots each with duration $T_b = \frac{T}{M}$. The MPPM data-word bits are used to describe the position of the $\omega = 4$ signal slots with the $M = 8$ time-slot frame. The control signal after the T-SPU monitors both the DC-bias and the OAM modulator ON and OFF operations. Every 4 bits are mapped into one OAM state from the 16 used OAM states for OAM modulation. The ωm bits (NOAM data part) are encoded in the ω signal time slots as a result of data manipulation. The modulator output is combined with the DC-biasing source output to power the laser diode (LD).

At the receiver side, a band-pass filter (BPF) is applied on the photodetector output to eliminate noise and interference, thus improving the signal quality. The 3-dB coupler then divides the BPF output into two parts. After being incorporated over each time slot, the upper arm signal is sent to the receiver-SPU (R-SPU). An analog-to-digital converter preserves the performance in the R-SPU. The N accumulated levels are ordered in decreasing order to evaluate the greatest levels of ω according to the time slots of the MPPM symbol signal. The MPPM symbols are then decoded by the R-SPU using a map of MPPM symbols to bits. On the other arm, an NOAM demodulator completes the decoding step after a fixed two-frame time delay thread. The R-SPU has enough time to determine the positions of the ω utmost level time slot because of this delay. NOAM symbols can be found in these time slots. The R-SPU then decodes the NOAM symbols chosen from an NOAM symbols-to-bits diagram. Finally, the received data words are obtained.

B. ANALYSIS FOR THE BER OF NOAM-MPPM

To get the BER of NOAM-MPPM through FSO channel, the following steps are followed:

1) COMPUTING THE PARAMETERS OF THE USED CHANNEL

The parameters of the channel are derived by the following steps. The probability density function (pdf) of a $\Gamma\Gamma$ turbulence channel with PE is given by [36]:

$$f_I(I) = \int f_{I|I_a}(I|I_a) f_{I_a}(I_a) dI_a \tag{1}$$

where I is the channel fading coefficient due to both AT and PE, while I_a is the fading coefficient due to AT only. Here, $f_{I|I_a}(I|I_a))$ denotes the conditional pdf given an I_a state

$$f_{I|I_a}(I_a) = \frac{\gamma^2}{A_0^{\gamma^2} I_a} \left(\frac{I}{I_a}\right)^{\gamma^2-1}, \quad 0 \le I \le A_0 I_a \tag{2}$$

and $f_{I_a}(I_a)$ denotes the pdf of the $\Gamma\Gamma$ turbulence channel given by [37]:

$$f_{I_a}(I_a) = \frac{\chi^{\chi} B^B}{\Gamma(\chi)\Gamma(B)} I_a^{B-1} \int_0^{\infty} x^{\chi-B-1} e^{-\left(\chi x + \frac{BI_a}{x}\right)} dx \tag{3}$$

where A_0 is the percentage of the power gathered at zero radial distance, γ is the proportion of the identical beam radius to the standard deviation of PE displacement at the receiver, and χ and B are the amounts of small-scale and large-scale eddies of the scattering atmosphere, respectively, The combined pdf of $\Gamma\Gamma$ channel with PE is [36], [38]:

$$f_I(I) = \frac{\gamma^2}{A_0^{\gamma^2}} \frac{\chi^{\chi} B^B}{\Gamma(\chi)\Gamma(B)} I^{\gamma^2-1} W \tag{4}$$

where

$$W = \int_{\frac{I}{A_0}}^{\infty} \int_0^{\infty} x^{\chi-B-1} e^{-\left(\chi x + \frac{BI_a}{x}\right)} I_a^{B-\gamma^2-1} dx dI_a \tag{5}$$

From [36], the combined pdf of $\Gamma\Gamma$ with PE is given as:

$$f_I(I) = \frac{\gamma^2 (\chi B)^{\frac{\chi+B}{2}}}{A_0 \Gamma(\chi)\Gamma(B)} I^{\frac{\chi+B}{2}-1} A_0^{1-\frac{\chi+B}{2}} G_{1,3}^{3,0}\left[\frac{\chi B}{A_0} I \middle| \begin{matrix}\kappa_1 \\ \kappa_2\end{matrix}\right] \tag{6}$$

where $\kappa_1 = 1 - \frac{\chi+B}{2} + \gamma^2$ and $\kappa_2 = -\frac{\chi+B}{2} + \gamma^2$, $\frac{\chi-B}{2}$, $\frac{B-\chi}{2}$ Comparing (4) and (6), we get:

$$W = \left[\sqrt{\frac{BI}{\chi A_0}}\right]^{\chi-B} \left[\frac{I}{A_0}\right]^{B-\gamma^2} G_{1,3}^{3,0}\left[\frac{\chi B}{A_0} I \middle| \begin{matrix}\kappa_1 \\ \kappa_2\end{matrix}\right] \tag{7}$$

N independent and identically distributed observed data will represent the likelihood function for (χ, B, γ). $I = I_1, I_2, \cdots, I_N$, where N is the number of applied OAM states.

$$L(\chi, B, \gamma) = \frac{\gamma^{2N} \chi^{\chi N} B^{BN}}{A_0^{N\gamma^2} \Gamma^N(\chi)\Gamma^N(B)} \prod_{i=1}^{N} I_i^{\gamma^2-1} \prod_{i=1}^{N} W_i \tag{8}$$

Taking log of both sides of (8), we get:

$$\begin{aligned}\log[L(\chi, B, \gamma)] = {} & N\chi \log \chi + NB \log B + 2N \log \gamma \\ & - N\gamma^2 \log A_0 - N \log \Gamma(\chi) - N \log \Gamma(B) \\ & \times (\gamma^2 - 1) \sum_{i=1}^{N} \log I_i + \sum_{i=1}^{N} \log W_i\end{aligned} \tag{9}$$

Combining the partial derivatives of both parts of (9) with respect to χ, B, and γ, receptively, we get:

$$\begin{aligned}\frac{\partial}{\partial \chi} \log[L(\chi, B, \gamma)] &= \xi + \sum_{i=1}^{N} \left\{\frac{\frac{\partial}{\partial \chi} W_i}{W_i}\right\} \\ \frac{\partial}{\partial B} \log[L(\chi, B, \gamma)] &= \delta + \sum_{i=1}^{N} \left\{\frac{\frac{\partial}{\partial B} W_i}{W_i}\right\} \\ \frac{\partial}{\partial \gamma} \log[L(\chi, B, \gamma)] &= \upsilon + \sum_{i=1}^{N} \left\{\frac{\frac{\partial}{\partial \gamma} W_i}{W_i}\right\}\end{aligned} \tag{10}$$

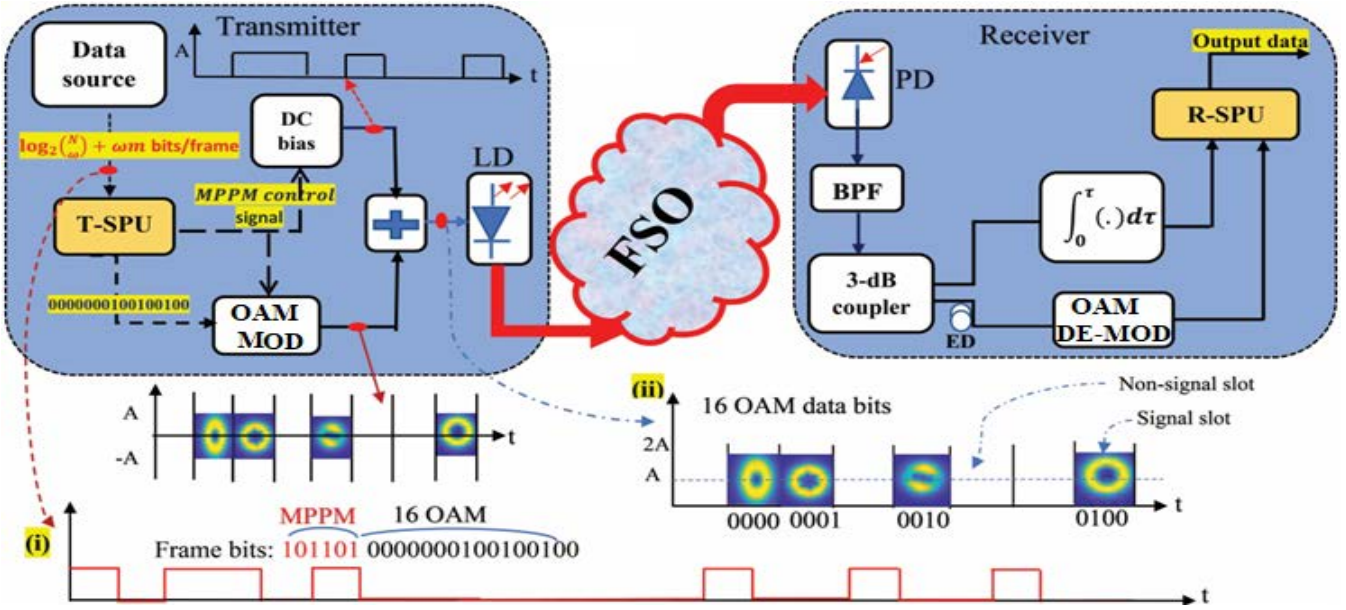

FIGURE 1. Schematic diagram of an FSO system using *N*OAM-MPPM technique in a ΓΓ turbulence channel with PE. LD: laser diode, PD: photodetector, ED: electronic delay, T(R)-SPU: transmitter (receiver) signal processing unit, MOD (DE): modulator and demodulator, BPF: band-pass filter, DC: direct current,. The time domain signal diagram for (i) the bits stream in a single frame and (ii) a transmitted NOAM-MPPM frame with ($N = 16$, $M = 8$, and $\omega = 4$).

where $\xi = N[\log\chi + 1 - \psi(\chi)]$, $\delta = N[\log B + 1 - \psi(B)]$, $\upsilon = 2N[1/\gamma - \gamma\log A_0] + 2\gamma\sum_{i=0}^{N}\log I_i$, $\psi(z) = \log(z) - 1/2z$ and $z \in \{\chi, B\}$.

The next step is to determine the partial derivatives $\{\frac{\partial}{\partial\chi}W_i, \frac{\partial}{\partial B}W_i, \frac{\partial}{\partial\gamma}W_i\}$ in order to evaluate the set of equations in (10). Then, we equate these equations to zero so as to determine the parameters (χ, B, γ) [38], [39]. Let

$$\frac{\partial}{\partial\chi}W_i = J_1 - J_2 \tag{11}$$

where

$$J_1 = \int_{\frac{I}{A_0}}^{\infty}\int_0^{\infty}\log(x)\,x^{\chi-B-1}e^{-\left(\chi x+\frac{BI_{a_i}}{x}\right)}I_{a_i}^{B-\gamma^2-1}dxdI_{a_i}$$
$$J_2 = \int_{\frac{I}{A_0}}^{\infty}\int_0^{\infty}x^{\chi-B}e^{-\left(\chi x+\frac{BI_{a_i}}{x}\right)}I_{a_i}^{B-\gamma^2-1}dx \tag{12}$$

According to [38], and [39], the solution for the previous equation can be found.

Let: $h(t,x) = \{I_{a_i}^{\chi-\gamma^2-1+t}e^{(-\chi x-\frac{BI_a}{x})}\}$

$$J_1 = \int_{\frac{I}{A_0}}^{\infty}\int_0^{\infty}x^{\chi-B-1}\log(x)\,e^{-(\chi x+\frac{BI_{a_i}}{x})}I_{a_i}^{B-\gamma^2-1}dxdI_{a_i}$$
$$= \int_{\frac{I}{A_0}}^{\infty}\left\{\int_0^{\infty}\frac{\partial}{\partial t}\left[x^{\chi-B-1}x^t e^{-(\chi x+\frac{BI_{a_i}}{x})}I_{a_i}^{B-\gamma^2-1}dxdI_{a_i}\right]\right\}$$
$$, t = 0 \tag{13}$$

Now: $J_1 = \frac{d}{dt}W$, with $t = 0$ as shown in (14) and (15) at the bottom of the next page where $T_1 = G_{1,3}^{3,0}\left[\frac{\chi B}{A_0}I\Big|_{\frac{\chi+B+t}{2}+\gamma^2,\frac{\chi-B+t}{2},-\frac{\chi-B+t}{2}}^{1-\frac{\chi+B+t}{2}+\gamma^2}.\right]$. The value of J_2 can be obtained in a similar way as that of J_1 with $t = 1$ as:

$$J_2 = \left[\sqrt{\frac{BI_i}{\chi A_0}}\right]^{\chi-B+1}\left[\frac{I_i}{A_0}\right]^{B-\gamma^2}T_2 \tag{16}$$

where $T_2 = G_{1,3}^{3,0}\left[\frac{\chi B}{A_0}I\Big|_{\frac{\chi+B+1}{2}+\gamma^2,\frac{\chi-B+1}{2},-\frac{\chi-B+1}{2}}^{1-\frac{\chi+B+1}{2}+\gamma^2}\right]$.

After getting J_1, and J_2, the value of $\frac{\partial}{\partial\chi}\log[L(\alpha,B,\gamma)]$ is obtained as:

$$\frac{\partial}{\partial\chi}\log[L(\chi,B,\gamma)]$$
$$= \xi + \sum_{i=1}^{N}\left[\log\sqrt{\frac{BI_i}{\chi A_0}} + \frac{\frac{\partial}{\partial t}T_1}{T_1}\right]$$
$$-\sum_{i=1}^{N}\sqrt{\frac{BI_i}{\chi A_0}}\frac{T_2}{T_1},\quad t = \chi - B. \tag{17}$$

$$J_3$$
$$= (-2\gamma).$$
$$\int_{\frac{I}{A_0}}^{\infty}\int_0^{\infty}\log(I_a).I_a^{B-\gamma^2-1}.x^{\chi-B-1}.e^{-(\chi x-\frac{BI_a}{x})}.dxdI_a$$
$$= (-2\gamma).\int_{\frac{I}{A_0}}^{\infty}\int_0^{\infty}\frac{\partial}{\partial t}$$
$$\times\left\{I_a^{B-\gamma^2-1+t}.x^{\chi-B-1}.e^{-(\chi x-\frac{BI_a}{x})}dxdI_a\right\}$$
$$= (-2\gamma).\frac{d}{dt}\left\{\int_{\frac{I}{A_0}}^{\infty}\int_0^{\infty}I_a^{B-\gamma^2-1+t}.x^{\chi-B-1}\right.$$
$$\left..e^{-(\chi x-\frac{BI_a}{x})}dxdI_a\right\}$$

$$= (-2\gamma).\frac{d}{dt}\left\{\left[\sqrt{\frac{BI_i}{\chi A_0}}\right]^{\chi-B}.\left[\frac{I_i}{A_0}\right]^{B-\gamma^2+t}.T\right\}$$

$$= (-2\gamma).\left[\sqrt{\frac{BI_i}{\chi A_0}}\right]^{\chi-B}$$

$$\left\{\left[\frac{I_i}{A_0}\right]^{B-\gamma^2+t}.\log\left(\frac{I_i}{A_0}\right).T+\left[\frac{I_i}{A_0}\right]^{B-\gamma^2+t}.\frac{\partial}{\partial t}T\right\},$$

$$t=0$$

J_3

$$= (-2\gamma).\left[\sqrt{\frac{BI_i}{\chi A_0}}\right]^{\chi-B}.\left[\frac{I_i}{A_0}\right]^{B-\gamma^2}.$$

$$\left\{\log\left(\frac{I_i}{A_0}\right).[T_1]+\frac{\partial}{\partial t}[T_1]\right\} \tag{18}$$

$$\frac{\partial}{\partial\gamma}\log[L(\chi,B,\gamma)]$$

$$= 2N\left[\frac{1}{\gamma}-\log(A_0)\right]+2\gamma\sum_{i=0}^{N}\log(I_i)$$

$$+\sum_{i=1}^{N}\left\{\frac{I_3}{\left[\sqrt{\frac{BI_i}{\chi A_0}}\right]^{\chi-B}.\left[\frac{I_i}{A_0}\right]^{B-\gamma^2}.[T_1]}\right\}$$

$$= 2N\left[\frac{1}{\gamma}-\log(A_0)\right]$$

$$+2\gamma\sum_{i=0}^{N}\log(I_i)+\sum_{i=1}^{N}\left\{(-2\gamma).\log\left(\frac{I_i}{A_0}\right)+\frac{\left[\frac{\partial}{\partial t}T_1\right]}{[T_1]}\right\}. \tag{19}$$

$$\frac{\partial W}{\partial B}$$

$$= \int_{\frac{I}{A_0}}^{\infty}\int_{0}^{\infty}-x^{\chi-B-1}.\log(x)\cdot e^{-(\chi x+\frac{BIa_i}{x})}.I_{a_i}^{B-\gamma^2-1}dxdI_{a_i}$$

$$+\int_{\frac{I}{A_0}}^{\infty}\int_{0}^{\infty}x^{\chi-B-1}\cdot e^{-(\chi x+\frac{BIa_i}{x})}.(\frac{-I_a}{x})\cdot I_{a_i}^{B-\gamma^2-1}dxdI_{a_i}$$

$$+\int_{\frac{I}{A_0}}^{\infty}\int_{0}^{\infty}x^{\chi-\beta-1}\cdot\log(I_{a_i})\cdot e^{-(\chi x+\frac{BIa_i}{x})}$$

$$.I_{a_i}^{B-\gamma^2-1}dxdI_{a_i}$$

$$= J_4+J_5+J_6 \tag{20}$$

J_4

$$= \int_{\frac{I}{A_0}}^{\infty}\int_{0}^{\infty}-\log(x).x^{\chi-B-1}.e^{(-\chi x-\frac{BI_a}{x})}.I_a^{B-\gamma^2-1}dxdI_a$$

$$= \int_{\frac{I}{A_0}}^{\infty}\int_{0}^{\infty}\frac{\partial}{\partial t}(-x)^{\chi-B-1+t}.e^{(-\chi x-\frac{BI_a}{x})}.I_a^{B-\gamma^2-1}dxdI_a$$

$$= \frac{d}{dt}$$

$$\left\{\int_{\frac{I}{A_0}}^{\infty}\int_{0}^{\infty}x^{\chi-B-1+t}\cdot e^{(-\chi x-\frac{BI_a}{x})}\cdot I_a^{B-\gamma^2-1}dxdI_a\right\}$$

$$= \left[\frac{I_i}{A_0}\right]^{B-\gamma^2}.\left[\sqrt{\frac{BI_i}{\chi A_0}}\right]^{\chi-B+t}.\log\left(\sqrt{\frac{BI_i}{\chi A_0}}\right).T$$

$$+\left[\sqrt{\frac{BI_i}{\chi A_0}}\right]^{\chi-B+t}.\frac{\partial}{\partial t}T,t=0 \tag{21}$$

J_4

$$= -\left[\frac{I_i}{A_0}\right]^{B-\gamma^2}.\left[\sqrt{\frac{BI_i}{\chi A_0}}\right]^{\chi-B}$$

$$.\left\{\log\left(\sqrt{\frac{BI_i}{\chi A_0}}\right).[T_1\}+\frac{\partial}{\partial t}T_1\right\} \tag{22}$$

J_5

$$= \int_{\frac{I}{A_0}}^{\infty}\int_{0}^{\infty}x^{\chi-B-1}.e^{-(\chi x-\frac{BI_a}{x})}.(\frac{-I_a}{x}).I_a^{B-\gamma^2-1}dxdI_a$$

$$= \int_{\frac{I}{A_0}}^{\infty}\int_{0}^{\infty}-x^{\chi-B-2}.e^{-(\chi x-\frac{BI_a}{x})}.I_a^{B-\gamma^2}dxdI_a. \tag{23}$$

J_5

$$= -\left\{\left[\sqrt{\frac{BI_i}{\chi A_0}}\right]^{\chi-B-1}.\left[\frac{I_i}{A_0}\right]^{B-\gamma^2+1}.[T_3]\right\} \tag{24}$$

$$J_1 = \frac{d}{dt}\left\{\int_{\frac{I}{A_0}}^{\infty}\int_{0}^{\infty}x^{\chi-B-1+t}.e^{(-\chi x-\frac{BI_a}{x})}.I_a^{B-\gamma^2-1}dxdI_a\right\}$$

$$= \frac{d}{dt}\left[\sqrt{\frac{BI_i}{\alpha A_0}}\right]^{\chi-B+t}.\left[\frac{I_i}{A_0}\right]^{B-\gamma^2}.[T] = \left[\frac{I_i}{A_0}\right]^{B-\gamma^2}.$$

$$\left\{\left[\sqrt{\frac{BI_i}{\chi A_0}}\right]^{\chi-B+t}.\log\left(\sqrt{\frac{BI_i}{\chi A_0}}\right).T+\left[\sqrt{\frac{BI_i}{\alpha A_0}}\right]^{\chi-B+t}.\frac{\partial}{\partial t}T\right\} \tag{14}$$

$$J_1 = \left[\frac{I_i}{A_0}\right]^{B-\gamma^2}.\left[\sqrt{\frac{BI_i}{\chi A_0}}\right]^{\chi-B}.\left\{\log\left(\sqrt{\frac{BI_i}{\chi A_0}}\right).T_1+\frac{\partial}{\partial t}T_1\right\} \tag{15}$$

where:

$$T_3 = G_{1,3}^{3,0}\left[\frac{\chi B}{A_0} I\Big|_{\frac{\chi+B-1}{2}+\gamma^2,\ \frac{\chi-B-1}{2},\ -(\frac{\chi-B-1}{2})}^{1-\frac{\chi+B-1}{2}+\gamma^2}\right]$$

$$\begin{aligned} J_6 &= \int_{\frac{I}{A_0}}^{\infty}\int_0^{\infty} \log(I_a).x^{\chi-B-1}.e^{(-\chi x-\frac{BI_a}{x})}.I_a^{B-\gamma^2-1}dxdI_a \\ &= \int_{\frac{I}{A_0}}^{\infty}\int_0^{\infty} \frac{\partial}{\partial t} I_a^{B-\gamma^2-1+t}.x^{\chi-B-1}.e^{-(\chi x-\frac{BI_a}{x})}dxdI_a \\ &= \frac{d}{dt}\left\{\int_{\frac{I}{A_0}}^{\infty}\int_0^{\infty} I_a^{B-\gamma^2-1+t}.x^{\chi-B-1}.e^{-(\chi x-\frac{BI_a}{x})}dxdI_a\right\} \\ &= \frac{d}{dt}\left\{\left[\sqrt{\frac{\beta I_i}{\alpha A_0}}\right]^{\chi-B}.\left[\frac{I_i}{A_0}\right]^{B-\gamma^2+t}.T\right\} \\ &= \left[\sqrt{\frac{BI_i}{\chi A_0}}\right]^{\chi-B}. \\ &\quad \left\{\left[\frac{I_i}{A_0}\right]^{B-\gamma^2+t}.\log\left(\frac{I_i}{A_0}\right).T + \left[\frac{I_i}{A_0}\right]^{B-\gamma^2+t}.\frac{\partial}{\partial t}T\right\}, \\ &\quad t=0 \end{aligned} \tag{25}$$

$$\begin{aligned} J_6 &= \left[\sqrt{\frac{BI_i}{\chi A_0}}\right]^{\chi-B}.\left[\frac{I_i}{A_0}\right]^{B-\gamma^2} \\ &\quad .\left\{\log\left(\frac{I_i}{A_0}\right).[T_1] + \frac{\partial}{\partial t}[T_1]\right\} \end{aligned} \tag{26}$$

$$\begin{aligned} \frac{\partial}{\partial B}\log[L(\chi,B,\gamma)] &= \delta \\ &\quad + \sum_{i=1}^{N}\frac{J_4+J_5+J_6}{\{\int_{\frac{I}{A_0}}^{\infty}\int_0^{\infty} x^{\chi-B-1}.e^{-(\chi x-\frac{BI_a}{x})}.I_a^{B-\gamma^2-1}dxdI_a\}} \\ &= \delta \\ &\quad + \sum_{i=1}^{N}\frac{J_4+J_5+J_6}{\{[\sqrt{\frac{BI_i}{\chi A_0}}]^{\chi-B}.[\frac{I_i}{A_0}]^{B-\gamma^2}.[T_1]\}} = \delta \\ &\quad + \sum_{i=1}^{N}\left[\sqrt{\frac{BI_i}{\chi A_0}}\right]^{\chi-B}.\left[\frac{I_i}{A_0}\right]^{B-\gamma^2} \\ &\quad \log\left(\frac{I_i}{A_0}\right).T_1 + \frac{\partial}{\partial t}[T_1] - \left\{\left[\sqrt{\frac{BI_i}{\chi A_0}}\right]^{-1}.[\frac{I_i}{A_0}]^1.[T_3]\right\} \\ &\quad - \left\{\log\left(\sqrt{\frac{BI_i}{\chi A_0}}\right).[T_1]\} + \{\frac{\partial}{\partial t}[T_1]\}\right\}.\frac{1}{Q} = \delta \\ &\quad + \sum_{i=1}^{N}\left\{\{\log(\frac{I_i}{A_0}).[T_1] + \frac{\partial}{\partial t}[T_1] \right. \\ &\quad \left. -\{[\sqrt{\frac{BI_i}{\chi A_0}}]^{-1}.[\frac{I_i}{A_0}]^1.[T_3]\}\right\} \\ &\quad -\{\{\log(\sqrt{\frac{BI_i}{\chi A_0}}).[T_1]\} + \{\frac{\partial}{\partial t}[T_1]\}\}\{[\frac{1}{T_1}]\}\} \\ &= \delta + \sum_{i=1}^{N}\left\{\left(\log\left[\sqrt{\frac{\chi I_i}{BA_0}}\right].\frac{T_3}{T_1}\right) - \left[\sqrt{\frac{\chi I_i}{BA_0}}\right]\right\} \end{aligned} \tag{27}$$

where:

$$\delta = N[\log(B) + 1 - \psi(B)],$$

$$Q = \left[\sqrt{\frac{BI_i}{\chi A_0}}\right]^{\chi-B}.\left[\frac{I_i}{A_0}\right]^{B-\gamma^2}.[T_1], \quad \psi(z) = \log(z) - \frac{1}{2z}$$

Now, we have:

$$\begin{aligned} \frac{\partial}{\partial B}\log[L(\chi,B,\gamma)] &= \delta + \sum_{i=1}^{N}\left\{\log\left[\sqrt{\frac{\chi I_i}{BA_0}}\right]\frac{T_3}{T_1} - \sqrt{\frac{\chi I_i}{BA_0}}\right\} \\ \frac{\partial}{\partial \gamma}\log[L(\chi,B,\gamma)] &= \upsilon + \sum_{i=1}^{N}(-2\gamma)\left\{\log\left(\frac{I_i}{A_0}\right) + \frac{\frac{\partial}{\partial t}T_1}{T_1}\right\} \end{aligned} \tag{28}$$

where $T_3 = G_{1,3}^{3,0}\left[\frac{\chi B}{A_0} I\Big|_{\frac{\chi+B-1}{2}+\gamma^2,\ \frac{\chi-B-1}{2},\ -\frac{\chi-B-1}{2}}^{1-\frac{\chi+B-1}{2}+\gamma^2}\right]$. Using [37], we have $T_2 = T_1\sqrt{\frac{\chi B}{A_0}I_i}$ and $T_3 = T_1\sqrt{\frac{A_0}{\chi B}I_i}$. Let $z_1 = \sum_{i=1}^{N}\frac{\frac{\partial}{\partial t}T_1}{T_1}$. Accordingly, (17) and (28) become:

$$\begin{aligned} N\left[1+\frac{1}{2\chi}\right] + \sum_{i=1}^{N}\log\sqrt{\frac{BI_i}{\chi A_0}} + z_1 - \sum_{i=1}^{N}\frac{BI_i}{A_0} &= 0 \\ N\left[1+\frac{1}{2B}\right] + \sum_{i=1}^{N}\left\{\log\left[\sqrt{\frac{\chi I_i}{BA_0}}\right]\sqrt{\frac{A_0}{\chi BI_i}}\right\} & \\ - \sum_{i=1}^{N}\sqrt{\frac{\chi I_i}{BA_0}} &= 0. \end{aligned}$$

By subtraction and addition of the two previous equations:

$$\begin{aligned} N\left[\frac{1}{2\chi}-\frac{1}{2B}\right] + \sum_{i=1}^{N}\left\{\log(\frac{B}{\chi}).\sqrt{\frac{A_0}{\chi BI_i}}\right\} + z_1 - \sum_{i=1}^{N}\left[\frac{BI_i}{A_0}\right] & \\ + \sum_{i=1}^{N}\left[\sqrt{\frac{\chi I_i}{BA_0}}\right] &= 0 \end{aligned} \tag{29}$$

$$\begin{aligned} N\left[2+\frac{1}{2\chi}+\frac{1}{2B}\right] + \sum_{i=1}^{N}\left\{\log\left(\frac{I_i}{A_0}\right).\sqrt{\frac{A_0}{\chi BI_i}}\right\} + z_1 & \\ - \sum_{i=1}^{N}\frac{BI_i}{A_0} - \sum_{i=1}^{N}\left[\sqrt{\frac{\chi I_i}{BA_0}}\right] &= 0 \end{aligned} \tag{30}$$

After simple mathematical manipulation of last two equations, we get:

$$N\left[1+\frac{1}{2B}\right] = \sum_{i=1}^{N}\sqrt{\frac{\chi I_i}{BA_0}} \tag{31}$$

Now, we can easily get the value of A_0 using different values of χ and B according to different AT strength cases and different OAM modes. After that, γ can also be obtained. Finally, the parameters of the channel are now ready for usage with the BER equations of *N*OAM, and hybrid *N*OAM-MPPM models.

2) BER DERIVATION FOR NOAM THROUGH THE USED CHANNEL

After deriving the parameters of the channel, the next step is to extract the BER equations of NOAM and the hybrid NOAM-MPPM system. The received signal can be claimed as $y = \eta Ix + N_i$ [1], where x represents the data transmitted $\{0, 1\}$, I represents the obtained irradiance, η is the opto-to-electric translation factor, and N_i is the additive white Gaussian noise (AWGN). The received irradiance is given from [1] as: $I = |\int u(r,\phi,z)u(r,\phi,z)rdrd\phi|^2$, where $u(r,\phi,z)$ is the spatial distribution of Laguerre-Gauss (LG) beam, and it is given by [3].

$$u_{LG(l_n,p)}(r,\phi,z)_n = \frac{D}{\left(1+\frac{z^2}{((\pi\omega_0^2)/\lambda)^2}\right)^{1/2}} e^{-\frac{ikr^2z}{2\left(z^2+((\pi\omega_0^2)/\lambda)^2\right)}} \cdot e^{-\frac{r^2}{\omega^2(z)}} \left(\frac{r\sqrt{2}}{\omega(z)}\right)^{|l|} {l_p}^{|l|}\left(\frac{2r^2}{\omega^2(z)}\right) e^{-il\phi} e^{ikz} \cdot e^{i(2p+|l|+1)\tan^{-1}\left(\frac{z}{(\pi\omega_0^2)/\lambda}\right)} \tag{32}$$

where D is a normalization constant, r is the radial distance from z, l is the intertwined helical phase front, p is the radial index, $p+1$ is the number of circular or ring regions, (r,ϕ,z) are the cylindrical coordinates, $k = 2\pi/\lambda$ is the wave number, λ is the wavelength, and ${l_p}^{|l|}$ is the generalized Laguerre polynomial. The beam radius of the fundamental Gaussian beam at distance z is given by:

$$\omega(z) = \omega_0\sqrt{1+(z/z_R)^2} \tag{33}$$

where ω_0 is the beam waist at $z = 0$.

The channel applied is the $\Gamma\Gamma$ turbulence channel with PE, which is the most generalized fading model for characterizing the AT, and its pdf is provided by [40]:

$$f_I(I) = \frac{\chi B\zeta^2}{A_0\Gamma(\chi)\Gamma(B)} G_{1,3}^{3,0}\left[\frac{\chi B}{A_0} I\middle|_{\zeta^2-1,\,\chi-1,\,B-1}^{\zeta^2}\right] \tag{34}$$

The instantaneous electrical SNR and average electrical SNR are given by [37]:

$$\begin{aligned} \digamma &= (\eta I)^2/N_0 \\ \mu &= (\eta E[I])^2/N_0 \end{aligned} \tag{35}$$

respectively. The average SNR is given by [37]:

$$\bar{\digamma} = \mu\frac{E[I^2]}{E^2[I]}. \tag{36}$$

After getting the values of $E[I]$ and $E[I^2]$, the average received SNR is given by:

$$\bar{\digamma} = \mu\frac{(\chi+1)(B+1)(1+\zeta^2)^2}{\chi B\zeta^2(2+\zeta^2)}. \tag{37}$$

We can now calculate the value of I as follows:

$$I = A_0\cdot\sqrt{\frac{\digamma}{\mu}}\cdot\frac{\zeta}{(\sqrt{1+\zeta^2})}. \tag{38}$$

Using this straightforward random variable transformation between I and $\digamma$, the resulting SNR pdf under the intensity modulated/direct detection (IM/DD) technique is provided by:

$$f_{\digamma}(\digamma) = \frac{C}{\sqrt{\digamma}\Gamma(\chi)\Gamma(B)} G_{1,3}^{3,0}\left[\frac{\chi B\zeta^2}{\sqrt{1+\zeta^2}}\sqrt{\frac{\digamma}{\mu}}\middle|_{\kappa}^{\zeta^2+1}\right] \tag{39}$$

where $c = \sqrt{\mu(\zeta^2+1)}/A_0$ and $\kappa = \zeta^2-1, \chi-1, B-1$.

The signal that was initially broadcasted on OAM mode would expand to other OAM modes due to AT. The BER of NOAM can be calculated in a similar way as the SSK BER, and given as [12]:

$$\mathrm{BER}_{OAM}^{U} \le \frac{1}{N\log_2 N}\sum_{i=1}^{N}\sum_{j=1}^{N} d_H(b_i,b_j)\,\mathrm{PEP}^{i\to j} \tag{40}$$

where

$$\mathrm{PEP}^{i\to j} = Q\left[|I_i - I_j|\sqrt{\frac{\bar{\digamma}\log_2 N}{2}}\right] \tag{41}$$

where $\mathrm{PEP}^{i\to j}$, and $d_H(b_i,b_j)$ are the bit error probability and the Hamming distance between symbols b_i and b_j, respectively, $\bar{\digamma}$ is the average received SNR per bit, I_i and I_j are two channel gains that are distributed independently and identically and characterized by the $\Gamma\Gamma$ distribution, and $Q(\cdot)$ stands for the Gaussian Q-function.

The aim now is to obtain the value of $\mathrm{PEP}^{i\to j}$. Let $U = |I_i - I_j|$ and $Z = I_i - I_j$. Hence $U = |Z|$. The pdf of Z is given by [12]:

$$f_Z(Z) = \begin{pmatrix} \int_0^{\infty} f_{I_i}(Z+I_i).f_{I_i}(I_i)dI_i, for Z \ge 0 \\ \int_{-\infty}^{0} f_{I_i}(Z+I_i).f_{I_i}(I_i)dI_i, for Z < 0 \end{pmatrix} \tag{42}$$

The pdf of U is given by:

$$f_U(u) = f_Z(u) + f_Z(-u) \tag{43}$$

where: $f_Z(u) = f_Z(Z)$ for $Z \ge 0$ and $f_Z(-u) = f_Z(Z)$ for $Z < 0$.

Now, the value of $f_Z(Z)$ is:

$$f_Z(Z) = \int_0^{\infty} \frac{\chi B\zeta^2}{A_0.\Gamma(\chi).\Gamma(B)}.G_{1,3}^{3,0}\left[\frac{\chi B}{A_0}(I_i+Z)\middle|_{\kappa}^{\zeta^2}\right]. \frac{\chi B\zeta^2}{A_0.\Gamma(\chi).\Gamma(B)}.G_{1,3}^{3,0}\left[\frac{\chi B}{A_0}I_i\middle|_{\kappa}^{\zeta^2}\right] dI_i. \tag{44}$$

$$f_Z(Z) = \left(\frac{\chi B\zeta^2}{A_0\Gamma(\chi)\Gamma(B)}\right)^2 \int_0^{\infty} T_4T_5\,dI_i \tag{45}$$

where $T_4 = G_{1,3}^{3,0}\left[\frac{\chi B}{A_0}I_i\middle|_{\kappa}^{\zeta^2}\right]$ and $T_5 = G_{1,3}^{3,0}\left[\frac{\chi B}{A_0}(I_i+Z)\middle|_{\kappa}^{\zeta^2}\right]$. Letting $I = (\chi B/A_0)\,I_i$, we get:

$$f_Z(Z) = \frac{\chi B\zeta^4}{A_0(\Gamma(\chi)\Gamma(B))^2}\int_0^{\infty} G_{1,3}^{3,0}\left[I\middle|_{\kappa}^{\zeta^2}\right]$$

$$\times G_{1,3}^{3,0}\left[I+\frac{\chi B}{A_0}Z)\middle|\begin{matrix}\zeta^2\\ \kappa\end{matrix}\right]dI. \quad (46)$$

The solution for this integral can be found by comparing the previous equation with the following equation as [41]:

$$\int_0^\infty \tau^{\theta-1} \times G_{u,v}^{s,t}\left[\sigma+\tau\middle|\begin{matrix}c_1,\cdots,c_u\\ d_1,\cdots,d_v\end{matrix}\right] G_{p,q}^{m,n}\left[\omega\tau\middle|\begin{matrix}a_1,\cdots,a_p\\ b_1,\cdots,b_q\end{matrix}\right]d\tau = \sum_{k=0}^{\infty}\frac{(-\sigma)^k}{k!}\cdot G_{p+v,q+u+1}^{m+t,n+s+1}\left[\omega\middle|\begin{matrix}a\\ b\end{matrix}\right] \quad (47)$$

where $a = 1-\chi, a_1, \cdots, a_n, 1+k-\chi-d_v$ and $b = b_1, b_m, , \cdots, 1+k-\chi-c_u, 1+k-\chi$.

By comparison between (46), and (47), the following parameters are obtained: $\tau = I, \theta = \mathbf{1}, u = 1, v = 3, m = 3, n = 0, s = 3, t = 0, p = 1, q = 3, \sigma = \frac{1}{2}, \omega = 1, a_p = c_u = \zeta^2, d_v = b_q = \zeta^2 - 1, \chi - 1, B - 1, \sigma = \frac{\chi B}{A_0}.u$.

The solution of the integral in (46) is [41]:

$$f_Z(z) = f_Z(u) = \frac{\chi B\zeta^4}{A_0(\Gamma(\chi)\Gamma(B))^2}\sum_{k=0}^{\infty}\frac{\left(-\frac{\chi B}{A_0}u\right)^k}{k!}T_6, \quad (48)$$

where $T_6 = G_{5,5}^{3,4}\left[1\middle|\begin{matrix}0, 1+k-\zeta^2, 1+k-\chi, 1+k-B, \zeta^2\\ \zeta^2-1, \chi-1, B-1, k-\zeta^2, k\end{matrix}\right]$.

Similar calculations can be used to determine $f_Z(-u)$, with the result revealing that $f_Z(u) = f_Z(-u)$. Hence, pdf of U is:

$$f_U(U) = \frac{2.\chi B\zeta^4}{A_0(\Gamma(\chi)\Gamma(B))^2}\sum_{k=0}^{\infty}\frac{(-\frac{\chi B}{A_0}u)^k}{k!}T_6. \quad (49)$$

The average PEP can be calculated using:

$$\text{APEP}^{i\to j} = \int_0^\infty Q\left[u\sqrt{\frac{\bar{F}\log_2 N}{2}}\right]f_U(U)du \quad (50)$$

where $Q(x) = \frac{1}{2}\,erfc(\frac{x}{\sqrt{2}})$ and $erfc(\cdot)$ is the complementary error function.

Accordingly,

$$\text{APEP}^{i\to j} = \frac{\chi B\zeta^4}{A_0(\Gamma(\chi)\Gamma(B))^2}\sum_{k=0}^{\infty}\frac{(-\frac{\chi B}{A_0})^k}{k!}T_6 \times\int_0^\infty u^k\, erfc\left(\frac{u\sqrt{\bar{F}\log_2 N}}{2}\right)du. \quad (51)$$

Using $\int_0^\infty (x)^{a-1}\, erfc(bx)dx = \frac{\Gamma(\frac{a+1}{2})}{ab^a\sqrt{\pi}}$ [12], we get:

$$\text{APEP}^{i\to j} = \frac{\chi B\zeta^4}{A_0(\Gamma(\chi)\Gamma(B))^2}\sum_{k=0}^{\infty}\frac{(-\frac{\chi B}{A_0}u)^k}{k!}T_6 \times\frac{\Gamma(\frac{k+2}{2})}{(k+1)(\frac{\sqrt{\bar{F}\log_2 N}}{2})^a\sqrt{\pi}}. \quad (52)$$

Now, to obtain the average BER, the Hamming distance value is replaced by:

$$\frac{1}{N\log_2 N}\sum_{i=1}^{N}\sum_{j=1}^{N}d_H(b_i,b_j) = \frac{1}{N\log_2 N}\frac{N^2\log_2 N}{2} = \frac{N}{2}. \quad (53)$$

Accordingly,

$$\text{BER} = \frac{\chi B\zeta^4 N}{2A_0(\Gamma(\chi)\Gamma(B))^2}\sum_{k=0}^{\infty}\frac{(-\frac{\chi B}{A_0})^k}{k!}T_6 \times\frac{\Gamma(\frac{k+2}{2})}{(k+1)(\frac{\sqrt{\bar{F}\log_2 N}}{2})^{k+1}\sqrt{\pi}}. \quad (54)$$

3) DERIVATION A BER EQUATION FOR THE HYBRID NOAM-MPPM

The BER for the NOAM-MPPM scheme is calculated as the average of the BERs for both NOAM and MPPM schemes [6], [16]:

$$\text{BER} = \frac{\log_2\binom{M}{\omega}}{\log_2\binom{M}{\omega}+\omega m}\text{BER}_{\text{MPPM}} + \frac{\omega m}{\log_2\binom{M}{\omega}+\omega m} \times\left\{\text{BER}_{\text{OAM}}(1-\text{SER}_{\text{MPPM}}) + \frac{\text{SER}_{\text{MPPM}}}{2}\right\}. \quad (55)$$

We find estimates of upper bounds on BER_{MPPM} and SER_{MPPM} as follows [6]:

$$\text{BER}_{\text{MPPM}} \le \left\{\frac{2^{\lfloor\log_2\binom{M}{\omega}-1\rfloor}}{2^{\lfloor\log_2\binom{M}{\omega}\rfloor}-1}\right\}\text{SER}_{\text{MPPM}}. \quad (56)$$

To get SER_{MPPM}, we start by evaluating $\text{SER}_{\text{MPPM}}(F)$ for a given F.

$$\text{SER}_{\text{MPPM}}(F) \le \left[\frac{\binom{M}{\omega}-1}{2\sqrt{\pi}}\right]G_{1,2}^{2,0}\left[\frac{F\log_2\binom{M}{\omega}}{4N}\middle|\begin{pmatrix}1\\ \frac{1}{2},0\end{pmatrix}\right]. \quad (57)$$

Next, SER_{MPPM} is upper bounded as:

$$\begin{aligned}\text{SER}_{\text{MPPM}} &= \int_0^\infty \text{SER}_{\text{MPPM}}(F)f_F(F)dF\\ &\le \left[\frac{\binom{M}{\omega}-1}{4\sqrt{\pi}}\right]\frac{C}{\Gamma(\chi)\Gamma(B)}\int_0^\infty F^{-0.5}\\ &\quad\times G_{1,2}^{2,0}\left[(\frac{F\log_2\binom{M}{\omega}}{4N})\middle|\begin{pmatrix}1\\ \frac{1}{2},0\end{pmatrix}\right]\\ &\quad\times G_{1,3}^{3,0}\left[\frac{\chi B\zeta^2}{(\sqrt{1+\zeta^2})}\sqrt{\frac{F}{\mu}}\middle|\begin{pmatrix}\zeta^2+1\\ \zeta^2,\chi,B\end{pmatrix}\right]d\gamma.\end{aligned} \quad (58)$$

We get the following parameters by comparing the previous and the following equations [41]:

$$\int_0^\infty \tau^{\theta-1}G_{u,v}^{s,t}\left[\sigma\tau\middle|\begin{matrix}c_1,\cdots,c_u\\ d_1,\cdots,d_v\end{matrix}\right]G_{p,q}^{m,n}\left[\omega\tau^r\middle|\begin{matrix}a_1,\cdots,a_p\\ b_1,\cdots,b_q\end{matrix}\right]d\tau$$

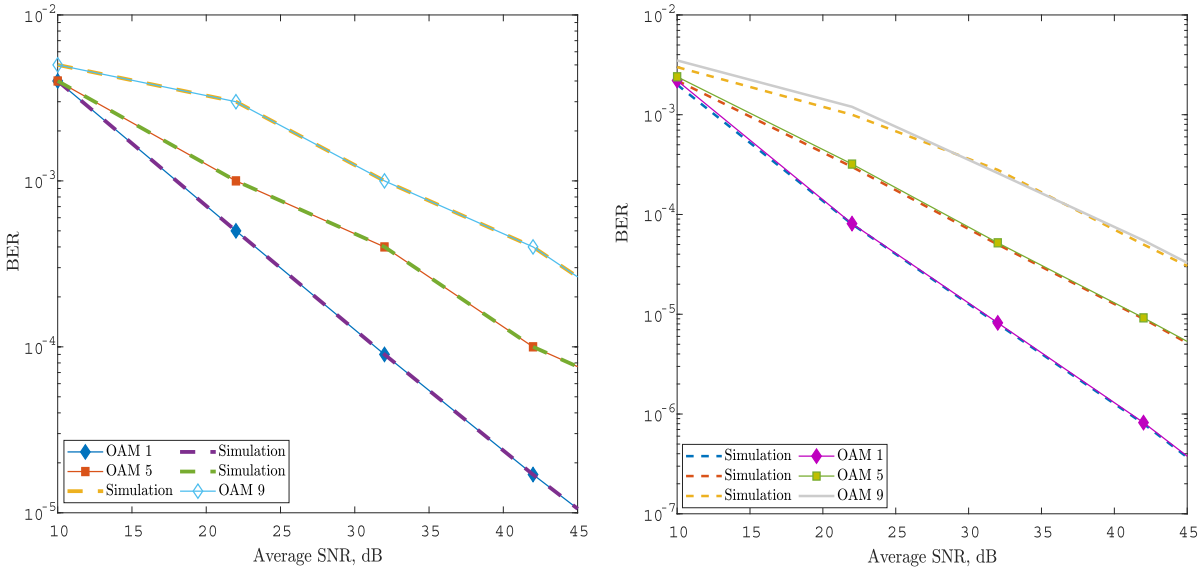

FIGURE 2. BER versus average received SNR under low turbulence strength: (a) OAM. (b) OAM + MPPM.

$$= \sigma^{-\theta} H_{p+v,q+u}^{m+t,n+s}\left[\frac{\omega}{\sigma^r}\middle|\begin{matrix}(a_1,1),\cdots,(a_p,1)\\(b_1,1),\cdots,(b_q,1)\end{matrix}\right]$$
$$= \frac{k^{\mu}.l^{(v-u)\theta+\rho-1}}{2\pi^{(k-1)c+(l-1)b}}\sigma^{-\theta} \times G_{kp+lv,kq+lu}^{km+lt,kn+ls}\left[\frac{\omega^k k^{k(p-q)}}{\sigma^l.l^{l(u-v)}}\middle|\begin{matrix}\frac{a_1}{k},\ldots,\frac{a_n}{k},\cdots,\frac{a_p+k-1}{k}\\ \frac{b_1}{k},\ldots,\frac{b_m}{k},\cdots,\frac{b_q+k-1}{k}\end{matrix}\right] \quad (59)$$

$\tau = \gamma, \theta = \frac{1}{2}, u = 1, v = 2, s = 2, t = 0, p = 1, q = 3, m = 3, n = 0, \omega = \frac{\alpha B\zeta^2}{\sqrt{\mu}.(\sqrt{1+\zeta^2})}, \sigma = \frac{\log_2\binom{N}{\omega}}{4N}, r = \frac{1}{2} = \frac{l}{k}, c_1 = 1, d_1 = 0, d_2 = \frac{1}{2}, a_1 = \zeta^2+1, b_1 = \zeta^2, b_2 = \chi, b_3 = B$

After comparing the two previous equations, we get:

$$\mathrm{SER}_{\mathrm{MPPM}} \le K_{\Upsilon}\left[\frac{2^{\chi+B-1}}{(2\pi)^1}\right] \times G_{4,7}^{6,2}\left[\frac{(\chi B\zeta^2)^2 N}{4\mu(\zeta^2+1)\log_2\binom{M}{\omega}}\middle| \times\left(\begin{matrix}\frac{\zeta^2+1}{2},\frac{\zeta^2+2}{2},\frac{1}{2},1\\ \frac{\zeta^2}{2},\frac{\zeta^2+1}{2},\frac{\chi}{2},\frac{B}{2},\frac{\chi+1}{2},\frac{B+1}{2},0\end{matrix}\right)\right] \quad (60)$$

where $K_{\Upsilon} = \left[\frac{\binom{M}{\omega}-1}{4\sqrt{\pi}}\right]\frac{2C}{\Gamma(\chi)\Gamma(B)}\left[\sqrt{\frac{N}{\log_2\binom{M}{\omega}}}\right]$.

Finally, we get the upper bound shown in (61), as shown at the bottom of the next page. where the Fox's H function is illustrated in [42].

C. PDF MODEL OF INTERMODAL CROSSTALK

Because of the turbulence, the attenuation and crosstalk would become OAM-dependent random variables. The empirical PDFs of attenuation and crosstalk are mostly influenced by turbulence strength and OAM mode [5]. When the transmitted power is conveyed by vortex light with OAM mode m, the attenuation and crosstalk $\eta_{m\to n}$ describe the fraction of power received on OAM mode n. According to [25], two crosstalk statistical models are used:

1) The generalized gamma distribution (GGD) can be used to represent crosstalk in the first model, and the analytical relations between the parameters of pdf and the turbulence strength are estimated as:

$$a(c_n^2, m, n) = a_{m\to n},$$
$$b(c_n^2, m, n) = b_{m\to n}^1 e^{-b_{m\to n}^2 c_n^2} + b_{m\to n}^3,$$
$$\mathrm{c}(c_n^2, m, n) = c_{m\to n}^1 (c_n^2)^2 + c_{m\to n}^2 c_n^2 + c_{m\to n}^3$$

2) The second model lowers the crosstalk distribution to an exponential distribution, and c_n^2 is linear to b.

where a, b, and c are the PDF parameters. The parameters of the OAM crosstalk pdf model are then determined using optimization methods. The trust region approach can be used in the future work to tackle the challenges of parameters.

D. RESULTS AND PERFORMANCE COMPARISON

In this section, our theoretical results are evaluated using Mathematica. In addition, these theoretical results are validated using Monte Carlo simulations (Matlab). Different turbulence parameters are shown in Table 1.

Figure 2 shows a comparison between the average BER versus SNR for different OAM states under low turbulence strength. It is indicated from the figure that the utilization of OAM plus MPPM improves the performance of the model by nearly five orders of magnitude compared to the utilization of OAM only. The reason for this improvement is that hybrid NOAM-MPPM systems have higher instantaneous

TABLE 1. Turbulence parameters.

Parameters	Values		
	Low	Moderate	Strong
Turbulence strength	10^{-15}	10^{-14}	10^{-13}
χ	11.6	4	4.2
B	10	1.9	1.3
Variance	0.2	1.6	3.5
Propagation distance	600 m		
ω_0	1.6 cm		
λ	1550 nm		
ω	4		
λ	1550 nm		
M	8		
λ	1550 nm		
SNR	0 to 45 dB		

TABLE 2. Average BER values for different OAM states.

Turbulence strength	SNR Values (dB)			
	10	20	30	40
Moderate	0.266	0.116	0.037	0.012
Strong	0.316	0.126	0.07	0.053

SNRs than those of the corresponding ordinary NOAM systems, when transmitting comparable data rates over the same bandwidth at a specific average SNR with a specific average optical power, resulting in a reduction in the BER of the NOAM part in the hybrid scheme compared to the ordinary NOAM scheme. Ordinary MPPM raises the number of signal slots to increase the amount of bits per symbol in order to maintain a comparable data rate constraint as compared to ordinary MPPM under the same conditions. As a result, when compared to the hybrid scheme, the standard MPPM SER rises. In addition, it is shown that both theoretical and simulation results are nearly the same under different SNR values.

Figure 3 shows a comparison between the average BER of OAM versus SNR for different OAM states and turbulence conditions. The average BERs for different OAM states are shown in Table 2.

From the figure, it is worth noting that the theoretical and simulation results are extremely similar. OAM mode of order $m = +1$ achieves the lowest BER value compared to those of other modes with different orders at different AT levels. Specifically, for an OAM of order $+1$, the BERs for moderate and strong turbulence strengths reach values of nearly 4×10^{-6} and 1×10^{-4}, respectively, at an SNR of 80 dB. Increasing the order of the OAM mode causes the BER to increase. This is attributed to the fact that the OAM mode of order $m = +1$ is the least affected by AT, and its power distribution remains largely unchanged [1].

TABLE 3. Comparison between different receivers.

Modulator	Propagation distance				
	200	400	600	800	1000
CNN	2×10^{-11}	3×10^{-6}	10^{-5}	10^{-4}	0.001
Regular	10^{-11}	2×10^{-6}	10^{-5}	2×10^{-4}	0.003

TABLE 4. The accuracy of different sizes of datasets.

Dataset size	AE	RF	CNN
9000 images	100	99	83
6000 images	100	98	82
3000 images	100	98	81
1500 images	95	76	72
150 images	92	71	71

Figure 4 demonstrates a comparison between the average BERs of introduced *N*OAM-MPPM schemes using different OAM states at different AT levels. It is clear that a good matching between theoretical and simulation results exists. Again, under different AT conditions, the lowest BER value is achieved for an OAM of order $+1$. Specifically, the BERs of *N*OAM-MPPM-FSO system are nearly 2.2×10^{-10} and 1.67×10^{-7} for moderate and heavy turbulence levels, respectively, at an SNR of 80 dB.

From Figs. 3 and 4, it is clear that the proposed hybrid *N*OAM-MPPM system outperforms the conventional OAM systems significantly under different turbulence conditions and different OAM mode orders.

IV. COMPARATIVE STUDY BETWEEN CNN, RF, AND AE

The artificial intelligence (AI) algorithms are applied to enhance the detection model performance. Firstly, a comparison is made between the detection processes using both ordinary and AI receivers. The results show that both receivers have nearly the same performance, but with little improvement with AI using CNN as shown in Table 3.

After that, the learning accuracy with three different DL techniques is estimated on different datasets established from the hybrid *N*OAM-MPPM-FSO model. In the simulation study, the turbulence strengths are 10^{-15}, 10^{-14}, and 10^{-13} for low, moderate, and strong strength, respectively. In addition, the SNR values are also altered from 0 to 45 dB, and the signal power is set to a constant value that corresponds to the transmitted data amplitude. The noise power is adjusted based on the needed SNR. The propagation range is increased from 200 to 1000 m. The datasets are constructed using trial-and-error method for altering the dataset size until reaching the best one. Of course, at the beginning of simulation, the training is done using a large-size dataset as shown in Table 4. The accuracy of the model is high, but it takes a very long time in the training process. So, the size of dataset is reduced

$$\mathrm{SER}_{\mathrm{MPPM}} \leq K_{\Upsilon} H_{3,4}^{3,2}\left[\frac{2\alpha B\zeta^2}{(\sqrt{\mu(1+\zeta^2)})}\sqrt{\frac{N}{\log_2\binom{M}{\omega}}}\middle|\begin{pmatrix}(\zeta^2+1,1),(1,\frac{1}{2}),(\frac{1}{2},\frac{1}{2})\\(\zeta^2,1),(\chi,1),(B,1),(0,\frac{1}{2})\end{pmatrix}\right] \tag{61}$$

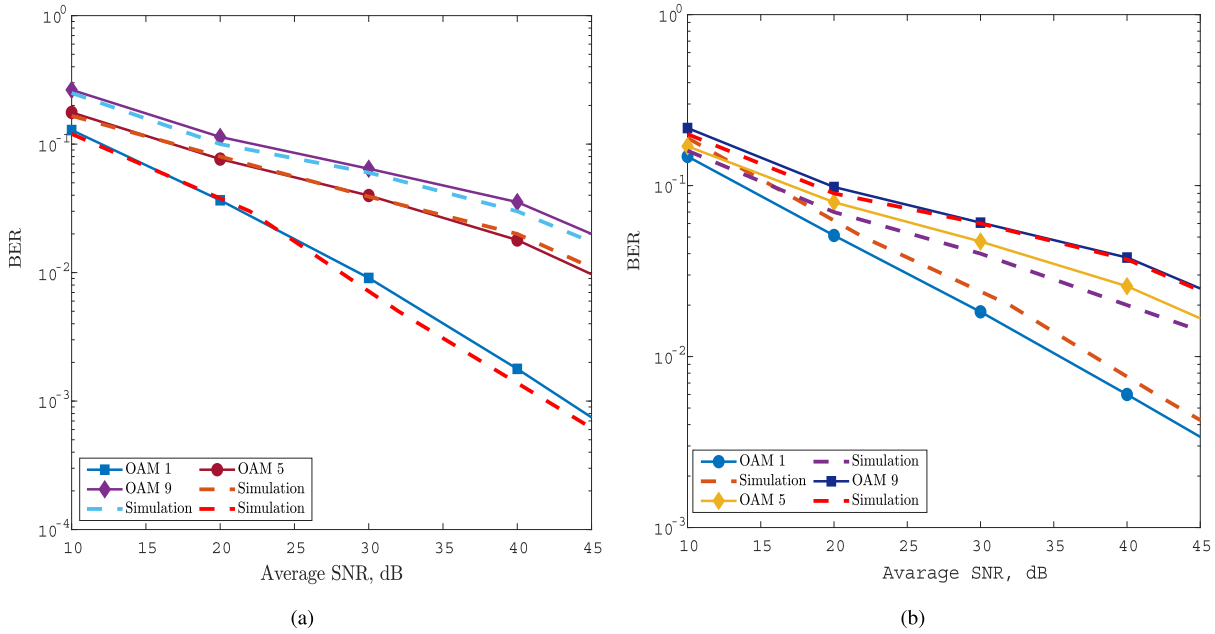

FIGURE 3. BER of OAM versus average received SNR under different turbulence strengths: (a) Moderate turbulence. (b) Strong turbulence.

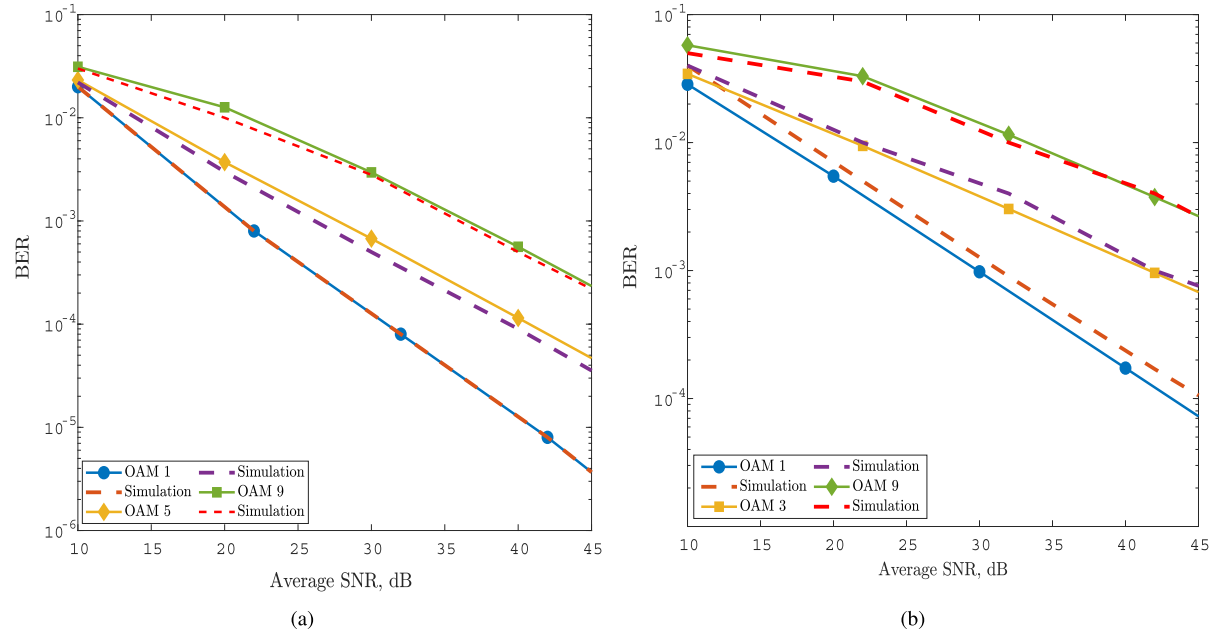

FIGURE 4. BER of hybrid NOAM-MPPM versus average received SNR under different turbulence strengths: (a) Moderate turbulence. (b) Strong turbulence.

for better performance of the model taking training time into account, and the results are shown as indicated in Table 5.

Three types of datasets are used and these datasets consist of 3 classes from the different OAM states (1, 3, and 5). Each class has a size of 1000, 500, or 50 images for large, moderate, and small datasets, respectively. After applying the three DL models (CNN, RF, and AE), it is concluded that the best dataset has a size of 150 images with 50 images in each class. The used datasets have a very small bias without nearly any over-fitting or under-fitting. The simulation results are obtained using 100 epochs, mini-batch size of 3, ADAM optimizer, a regularization factor of 0.0004 and a 0.0001 learning rate. The construction of the three DL techniques is indicated in Fig. 5.

In Tables 4 and 5, a comparative study between RF, AE, and CNN is presented using different datasets of the hybrid OAM-MPPM-FSO system. It is clear from the table that AE is the optimal DL technique for different used datasets (large, medium, and small). The AE has a value of 100% for PSNR, Recall [29], SP, Precision, AUC, FScore, and accuracy

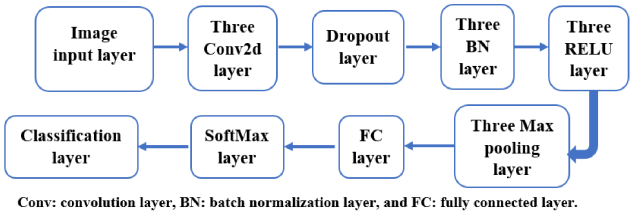

(a) CNN.

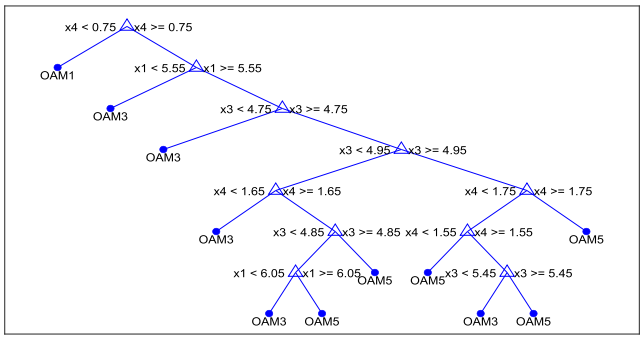

(b) Randomforest.

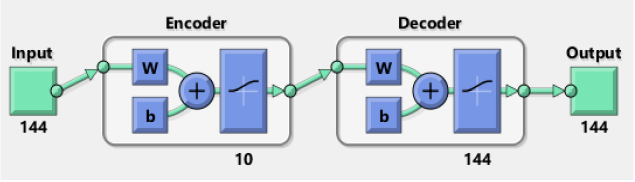

(c) Autoencoder.

FIGURE 5. Structure of the three proposed DL techniques.

TABLE 5. Different metrics of DL for the three proposed DL techniques.

Models	Dataset	Accuracy	RMSE	AUC	FScore	Precision	Recall	SP
AE	Small	92	0.15	96	22	88	100	92
	Medium	95	0.1	98	40	73	85	95
	Large	100	0.004	100	100	100	100	100
RF	Small	71	0.82	63	46	46	50	75
	Medium	76	0.6	66	39	37	50	81
	Large	98	0.04	98	98	98	98	98
CNN	Small	71	0.9	83	55	57	81	84
	Medium	72	0.7	83	56	58	82	84
	Large	81	0.4	84	74	72	80	87

for the large dataset size. In addition, the AE has the least RMSE followed by RF then CNN. From Table 4 and 5, it is shown that CNN with the different used datasets has the worst value for all metrics of DL compared to RF, and AE.

V. CONCLUSION AND FUTURE WORK

Closed-form expressions for ΓΓ channel with PE parameters and upper bounds on BERs have been extracted and studied for the FSO system using the hybrid *N*OAM-MPPM techniques. Under various turbulence levels and OAM states, the performance of an FSO system implementing *N*OAM-MPPM was compared to that of a system implementing ordinary OAM. The proposed *N*OAM-MPPM technique outperforms the standard OAM technique, according to our results. Specifically, BER improvements of orders about 10^{-5} and 10^{-3} are gained, when using the proposed *N*OAM-MPPM scheme, for both moderate and heavy turbulence channels, respectively. Moreover, we have concluded that to further enhance the performance of *N*OAM-MPPM FSO systems, three different DL classification techniques, namely AE, RF, and CNN can be used. AE has the best classification performance, optimal performance metrics of DL, and the lowest RMSE compared to the other models on different datasets of the *N*OAM-MPPM-FSO system.

As a future work, it will be beneficial to study OAM performance with other effective DL techniques in order to resolve faults in the OAM-SK optical system. Although our study focused on SISO OAM, all of the strategies established can be applied on the more efficient multiple input multiple output (MIMO) OAM. We will introduce theoretical analysis that can be easily used to approximate the performance of OAM with other modulation techniques. In the near future, it will also be useful to test our theoretical results using simulations on RSoft optSIM. Utilization of various encryption/decryption schemes with OAM-DL systems will be investigated to improve the efficiency and reliability of the systems. Several recent studies have looked into the performance of OAM mode recognition employing LG beams. In the future, we plan to investigate the performance of OAM mode recognition using Bessel Gaussian and hyper-geometric Gaussian beams.

ACKNOWLEDGMENT

Princess Nourah bint Abdulrahman University Researchers Supporting Project number (PNURSP2022R66), Princess Nourah bint Abdulrahman University, Riyadh, Saudi Arabia.

REFERENCES

[1] E.-M. Amhoud, B. S. Ooi, and M.-S. Alouini, "A unified statistical model for atmospheric turbulence-induced fading in orbital angular momentum multiplexed FSO systems," *IEEE Trans. Wireless Commun.*, vol. 19, no. 2, pp. 888–900, Feb. 2020.

[2] A. Trichili, K.-H. Park, M. Zghal, B. S. Ooi, and M.-S. Alouini, "Communicating using spatial mode multiplexing: Potentials, challenges, and perspectives," *IEEE Commun. Surveys Tuts.*, vol. 21, no. 4, pp. 3175–3203, 4th Quart., 2019.

[3] E.-M. Amhoud, A. Trichili, B. S. Ooi, and M.-S. Alouini, "OAM mode selection and space–time coding for atmospheric turbulence mitigation in FSO communication," *IEEE Access*, vol. 7, pp. 88049–88057, 2019.

[4] A. E. Morra, H. S. Khallaf, H. M. H. Shalaby, and Z. Kawasaki, "Performance analysis of both shot- and thermal-noise limited MultiPulse PPM receivers in gamma–gamma atmospheric channels," *J. Lightw. Technol.*, vol. 31, no. 19, pp. 3142–3150, Oct. 1, 2013.

[5] I. S. Ansari, F. Yilmaz, and M.-S. Alouini, "Performance analysis of FSO links over unified gamma–gamma turbulence channels," in *Proc. IEEE 81st Veh. Technol. Conf. (VTC Spring)*, May 2015, pp. 1–5.

[6] H. S. Khallaf, A. E. Elfiqi, H. M. H. Shalaby, S. Sampei, and S. S. A. Obayya, "On the performance evaluation of LQAM-MPPM techniques over exponentiated Weibull fading free-space optical channels," *Opt. Commun.*, vol. 416, pp. 41–49, Jun. 2018.

[7] H. Al-Quwaiee, I. S. Ansari, and M.-S. Alouini, "On the performance of free-space optical communication systems over double generalized gamma channel," *IEEE J. Sel. Areas Commun.*, vol. 33, no. 5, pp. 1829–1840, May 2015.

[8] F. S. Vetelino, C. Young, and L. Andrews, "Fade statistics and aperture averaging for Gaussian beam waves in moderate-to-strong turbulence," *Appl. Opt.*, vol. 46, no. 18, pp. 3780–3789, Jun. 2007.
[9] J. Zhang, M. Matthaiou, G. K. Karagiannidis, and L. Dai, "On the multivariate gamma–gamma distribution with arbitrary correlation and applications in wireless communications," *IEEE Trans. Veh. Technol.*, vol. 65, no. 5, pp. 3834–3840, May 2016.
[10] A. Bekkali, C. B. Naila, K. Kazaura, K. Wakamori, and M. Matsumoto, "Transmission analysis of OFDM-based wireless services over turbulent radio-on-FSO links modeled by gamma–gamma distribution," *IEEE Photon. J.*, vol. 2, no. 3, pp. 510–520, Jun. 2010.
[11] S. A. El-Meadawy, A. E. A. Farghal, H. M. H. Shalaby, N. A. Ismail, F. E. A. El-Samie, M. Abd-Elnaby, and W. El-Shafai, "Efficient and secure bit-level chaos security algorithm for orbital angular momentum modulation in free-space optical communications," *IEEE Access*, vol. 9, pp. 74817–74835, 2021.
[12] A. Jaiswal, M. R. Bhatnagar, and V. K. Jain, "Performance of optical space shift keying over gamma–gamma fading with pointing error," *IEEE Photon. J.*, vol. 9, no. 2, pp. 1–16, Apr. 2017.
[13] A. Al-Habash, L. C. Andrews, and R. L. Phillips, "Mathematical model for the irradiance probability density function of a laser beam propagating through turbulent media," *Opt. Eng.*, vol. 40, no. 8, pp. 1554–1563, Aug. 2001.
[14] B. Epple, "Simplified channel model for simulation of free-space optical communications," *J. Opt. Commun. Netw.*, vol. 2, no. 5, pp. 293–304, 2010.
[15] E. Agrell and M. Karlsson, "Power-efficient modulation formats in coherent transmission systems," *J. Lightw. Technol.*, vol. 27, no. 22, pp. 5115–5126, Nov. 15, 2009.
[16] H. Selmy, H. M. H. Shalaby, and Z.-I. Kawasaki, "Proposal and performance evaluation of a hybrid BPSK-modified MPPM technique for optical fiber communications systems," *J. Lightw. Technol.*, vol. 31, no. 22, pp. 3535–3545, Nov. 15, 2013.
[17] H. M. H. Shalaby, "Maximum achievable constrained power efficiencies of MPPM-*L* QAM techniques," *IEEE Photon. Technol. Lett.*, vol. 27, no. 12, pp. 1265–1268, Jun. 15, 2015.
[18] H. M. H. Shalaby, "Proposal of a power efficient *N*-level multipulse PPM-*L*QAM technique," *J. Lightw. Technol.*, vol. 38, no. 23, pp. 6542–6548, Dec. 1, 2020.
[19] X. Liu, S. Chandrasekhar, T. H. Wood, R. W. Tkach, P. J. Winzer, E. C. Burrows, and A. R. Chraplyvy, "M-ary pulse-position modulation and frequency-shift keying with additional polarization/phase modulation for high-sensitivity optical transmission," *Opt. Exp.*, vol. 19, no. 26, pp. B868–B881, 2011.
[20] H. Selmy, H. M. H. Shalaby, and Z. Kawasaki, "Enhancing optical multipulse pulse position modulation using hybrid BPSK-modified MPPM," in *Proc. CLEO*, 2013, pp. 1–2.
[21] H. S. Khallaf, H. M. H. Shalaby, and Z. Kawasaki, "Proposal of a hybrid OFDM-PPM technique for free space optical communications systems," in *Proc. IEEE Photon. Conf.*, Sep. 2013, pp. 287–288.
[22] H. S. Khallaf and H. M. H. Shalaby, "Proposal of a hybrid QAM-MPPM technique for optical communications systems," in *Proc. 16th Int. Conf. Transparent Opt. Netw. (ICTON)*, Jul. 2014, pp. 1–4.
[23] J. Li, M. Zhang, D. Wang, S. Wu, and Y. Zhan, "Joint atmospheric turbulence detection and adaptive demodulation technique using the CNN for the OAM-FSO communication," *Opt. Exp.*, vol. 26, no. 8, pp. 10494–10508, 2018.
[24] M. Dong, L. Yao, X. Wang, B. Benatallah, C. Huang, and X. Ning, "Opinion fraud detection via neural autoencoder decision forest," *Pattern Recognit. Lett.*, vol. 132, pp. 21–29, Apr. 2020.
[25] Y. Pan, P. Wang, W. Wang, S. Li, M. Cheng, and L. Guo, "Statistical model for the weak turbulence-induced attenuation and crosstalk in free space communication systems with orbital angular momentum," *Opt. Exp.*, vol. 29, no. 8, pp. 12644–12662, 2021.
[26] J. A. Anguita, M. A. Neifeld, and B. V. Vasic, "Modeling channel interference in an orbital angular momentum-multiplexed laser link," *Proc. SPIE*, vol. 7464, Aug. 2009, Art. no. 74640U.
[27] S. A. El-Meadawy, H. M. Shalaby, N. A. Ismail, F. E. A. El-Samie, and A. E. Farghal, "Free-space 16-ary orbital angular momentum coded optical communication system based on chaotic interleaving and convolutional neural networks," *Appl. Opt.*, vol. 59, no. 23, pp. 6966–6976, 2020.
[28] J. Liu, P. Wang, X. Zhang, Y. He, X. Zhou, H. Ye, Y. Li, S. Xu, S. Chen, and D. Fan, "Deep learning based atmospheric turbulence compensation for orbital angular momentum beam distortion and communication," *Opt. Exp.*, vol. 27, no. 12, pp. 16671–16688, 2019.
[29] H. E. Nistazakis, A. N. Stassinakis, S. S. Muhammad, and G. S. Tombras, "BER estimation for multi-hop RoFSO QAM or PSK OFDM communication systems over gamma gamma or exponentially modeled turbulence channels," *Opt. Laser Technol.*, vol. 64, pp. 106–112, Dec. 2014.
[30] H. Nistazakis, A. Stassinakis, H. Sandalidis, and G. Tombras, "QAM and PSK OFDM RoFSO over *M*-turbulence induced fading channels," *IEEE Photon. J.*, vol. 7, no. 1, pp. 1–11, Feb. 2014.
[31] P. Wang, B. Yang, L. Guo, and T. Shang, "SER performance analysis of MPPM FSO system with three decision thresholds over exponentiated Weibull fading channels," *Opt. Commun.*, vol. 354, pp. 1–8, Nov. 2015.
[32] G. Xu and Z. Song, "Performance analysis for mixed κ-μ fading and M-distribution dual-hop radio frequency/free space optical communication systems," *IEEE Trans. Wireless Commun.*, vol. 20, no. 3, pp. 1517–1528, Mar. 2021.
[33] G. Xu and Z. Song, "Performance analysis of a UAV-assisted RF/FSO relaying systems for internet of vehicles," *IEEE Internet Things J.*, early access, Jan. 12, 2021, doi: 10.1109/JIOT.2021.3051211.
[34] Z. Xu, G. Xu, and Z. Zheng, "BER and channel capacity performance of an FSO communication system over atmospheric turbulence with different types of noise," *Sensors*, vol. 21, no. 10, p. 3454, May 2021.
[35] G. Xu, Z. Song, and Q. Zhang, "Outage probability and channel capacity of an optical spherical wave propagating through anisotropic weak-to-strong oceanic turbulence with Málaga distribution," *J. Opt. Soc. Amer. A, Opt. Image Sci.*, vol. 37, pp. 1622–1629, Oct. 2020.
[36] C. Chen, H. Yang, Y. Lou, and S. Tong, "Changes in orbital-angular-momentum modes of a propagated vortex Gaussian beam through weak-to-strong atmospheric turbulence," *Opt. Exp.*, vol. 24, no. 7, pp. 6959–6975, Apr. 2016.
[37] M. Kazeminia and M. Mehrjoo, "A new method for maximum likelihood parameter estimation of gamma–gamma distribution," *J. Lightw. Technol.*, vol. 31, no. 9, pp. 1347–1353, May 1, 2013.
[38] H. G. Sandalidis, T. A. Tsiftsis, and G. K. Karagiannidis, "Optical wireless communications with heterodyne detection over turbulence channels with pointing errors," *J. Lightw. Technol.*, vol. 27, no. 20, pp. 4440–4445, Oct. 15, 2009.
[39] F. W. Olver, D. W. Lozier, R. F. Boisvert, and C. W. Clark, *NIST Handbook of Mathematical Functions Hardback and CD-ROM*. Cambridge, U.K.: Cambridge Univ. Press, 2010.
[40] M. Kazeminia and M. Mehrjoo, "A two-dimensional maximum likelihood parameter estimation of gamma–gamma distribution for free space optical channels with weak turbulence conditions," in *Proc. 6th Int. Symp. Telecommun. (IST)*, 2012, pp. 489–493.
[41] A. P. Prudnikov, I. A. Brychkov, and O. I. Marichev, *Integrals and Series: Special Functions*, vol. 3. Boca Raton, FL, USA: CRC Press, 1986.
[42] C. Fox, "The *G* and *H* functions as symmetrical Fourier kernels," *Trans. Amer. Math. Soc.*, vol. 98, no. 3, pp. 395–429, 1961.
[43] L. Darwesh and N. S. Kopeika, "Deep learning for improving performance of OOK modulation over FSO turbulent channels," *IEEE Access*, vol. 8, pp. 155275–155284, 2020.

SHIMAA A. EL-MEADAWY received the B.Sc. and M.Sc. degrees in electrical engineering from the Faculty of Electronic Engineering, Menoufia University, Menouf, Egypt, in 2013 and 2017, respectively, where she is currently pursuing the Ph.D. degree in electrical engineering. She is also an Assistant Lecturer with the Department of Electrical Engineering, Faculty of Electronic Engineering, Menoufia University. Her current research interests include optical communications, deep learning (DL) applications and computer vision, deep neural networks, information theory, elastic optical networks, image and video signal processing, efficient 2D video/3D multi-view video coding, multi-view video plus depth coding, 3D multi-view video coding and transmission, quality of service and experience, digital communication techniques, speech processing, and security algorithms.

HOSSAM M. H. SHALABY (Senior Member, IEEE) was born in Giza, Egypt, in 1961. He received the B.S. and M.S. degrees in electrical engineering from Alexandria University, Alexandria, Egypt, in 1983 and 1986, respectively, and the Ph.D. degree in electrical engineering from the University of Maryland at College Park, in 1991. In 1991, he joined the Electrical Engineering Department, Alexandria University, and was promoted to a Professor, in 2001. From 1996 to 1998, he was with the Electrical and Computer Engineering Department, International Islamic University Malaysia. From 1998 to 2001, he was with the School of Electrical and Electronic Engineering, Nanyang Technological University, Singapore. From December 2000 to 2004, he was an Adjunct Professor with the Department of Electrical and Information Engineering, Faculty of Sciences and Engineering, Laval University, Quebec, QC, Canada. He worked as a Consultant at SysDSoft Company, Alexandria, from 2007 to 2010. From 2010 to 2016, he was the Chair of the ECE Department, E-JUST. Since 2017, he has been on leave from Alexandria University, where he is currently a Professor with the Department of Electronics and Communications Engineering (ECE), School of Electronics, Communications, and Computer Engineering, Egypt-Japan University of Science and Technology (E-JUST), New Borg EL-Arab City, Alexandria, Egypt. His research interests include optical communications, silicon photonics, optical CDMA, and quantum information theory. Since 2020, he has been serving as a Student Branch Counselor for the IEEE E-JUST Student Branch.

NABIL A. ISMAIL received the Ph.D. degree in computer engineering from Durham University, U.K., in 1983. From August 2006 to August 2008, he was the Dean of the Faculty of Computers and Information, Menoufia University. He is currently a Professor of computer science and engineering with the Faculty of Electronic Engineering, Menoufia University. His main research interests include deep learning applications and computer vision, tomography, computer security, computer architecture, elliptic curve cryptography, processor design, light-power smart devices, security applications, EIT algorithms, and multi-core/many-core parallel programming.

FATHI E. ABD EL-SAMIE received the B.Sc. (Hons.), M.Sc., and Ph.D. degrees from Menoufia University, Menouf, Egypt, in 1998, 2001, and 2005, respectively. Since 2005, he has been a Teaching Staff Member with the Department of Electronics and Electrical Communications, Faculty of Electronic Engineering, Menoufia University. His current research interests include image enhancement, image restoration, image interpolation, super-resolution reconstruction of images, data hiding, multimedia communications, medical image processing, optical signal processing, and digital communications. He was a recipient of the Most Cited Paper Award from the *Digital Signal Processing* journal in 2008.

NAGLAA F. SOLIMAN received the B.Sc., M.Sc., and Ph.D. degrees from the Faculty of Engineering, Zagazig University, Egypt, in 1999, 2004, and 2011, respectively. Since 2015, she has been working with the Faculty of Computer Science, PNU, Saudi Arabia. She has been a Teaching Staff Member with the Department of Electronics and Communications Engineering, Faculty of Engineering, Zagazig University. Her current research interests include digital image processing, information security, multimedia communications, medical image processing, optical signal processing, big data, and cloud computing.

ABEER D. ALGARNI received the B.Sc. degree (Hons.) in computer science from King Saud University, Riyadh, Saudi Arabia, in 2007, and the M.Sc. and Ph.D. degrees from the School of Engineering and Computer Sciences, Durham University, U.K., in 2010 and 2015, respectively. Since 2008, she has been working as an Assistant Professor with the College of Computer and Information Sciences, Princess Nourah Bint Abdulrahman University. Her current research interests include networking and communication systems, digital image processing, digital communications, and cyber security.

WALID EL-SHAFAI was born in Alexandria, Egypt. He received the B.Sc. degree (Hons.) in electronics and electrical communication engineering from the Faculty of Electronic Engineering (FEE), Menoufia University, Menouf, Egypt, in 2008, the M.Sc. degree from the Egypt-Japan University of Science and Technology (E-JUST), in 2012, and the Ph.D. degree from the Faculty of Electronic Engineering, Menoufia University, in 2019. Since January 2021, he has been a Postdoctoral Research Fellow with the Security Engineering Laboratory (SEL), Prince Sultan University (PSU), Riyadh, Saudi Arabia. He is currently working as a Lecturer and an Assistant Professor with the Electronics and Communication Engineering (ECE) Department, FEE, Menoufia University. His research interests include wireless mobile and multimedia communications systems, image and video signal processing, efficient 2D video/3D multi-view video coding, multi-view video plus depth coding, 3D multi-view video coding and transmission, quality of service and experience, digital communication techniques, cognitive radio networks, adaptive filters design, 3D video watermarking, steganography, and encryption, error resilience and concealment algorithms for H.264/AVC, H.264/MVC, and H.265/HEVC video codecs standards, cognitive cryptography, medical image processing, speech processing, security algorithms, software defined networks, the Internet of Things, medical diagnoses applications, FPGA implementations for signal processing algorithms and communication systems, cancellable biometrics and pattern recognition, image and video magnification, artificial intelligence for signal processing algorithms and communication systems, modulation identification and classification, image and video super-resolution and denoising, cybersecurity applications, deep learning in signal processing, and communication systems applications. He has several publications in the above research areas in several reputable international and local journals and conferences. Also, he serves as a reviewer for several international journals.

AHMED E. A. FARGHAL received the B.Sc. (Hons.) and M.Sc. degrees in electrical engineering from Menoufia University, Menoufia, Egypt, in 2006 and 2011, respectively, and the Ph.D. degree in electrical engineering from the Egypt-Japan University for Science and Technology, Alexandria, Egypt, in 2015. In 2007, he joined the Department of Electronics and Electrical Communications Engineering, Faculty of Electronic Engineering, Menoufia University, and was promoted to a Lecturer Assistant, in 2011. From November 2014 to July 2015, he was a Special Research Student with Kyushu University, Fukuoka, Japan. He was with the Department of Electronics and Electrical Communications Engineering, Faculty of Electronic Engineering, Menoufia University, where he was an Assistant Professor. He is currently with the Electrical Engineering Department, Faculty of Engineering, Sohag University, Sohag, Egypt. His research interests include optical CDMA, all-optical networks, QoS provisioning in optical networks, elastic optical networking, green optical networks, and nano-optoelectronic devices.